The 4th European sCO_2 Conference for Energy Systems
March 23-24, 2021, Online Conference

2021-sCO2.eu-136

Design and off-design analysis of a highly loaded centrifugal compressor for sCO_2 applications operating in near-critical conditions

Alessandro Romei, Paolo Gaetani, Giacomo Persico
Laboratory of Fluid Machines
Energy Department, Politecnico di Milano
Via Lambruschini 4, Milano 20156

ABSTRACT

The closed gas cycle based on supercritical carbon dioxide (sCO_2) is a promising solution to realize highly efficient power systems arranged in compact devices. However, the technical feasibility of these so-called sCO_2 power systems relies on the development of non-conventional components, whose features are dictated by the peculiar character of the working fluid.

The compressor is a key component of the system and its design demands the set-up of novel guidelines, due to the near-critical thermodynamic condition of the fluid, which (i) makes the machine operate with a very low flow function, (ii) experiences steep changes in properties across the machine, and (iii) is prone to phase-change in the intake part of the machine.

In this study we revise the entire design workflow of a prototype sCO_2 centrifugal compressor, from the preliminary definition of the machine, to the mean-line design, and finally to the detailed definition of the meridional channel and of the blade shape, highlighting the aspects making the machine alternative to conventional ones. The compressor aerodynamics is then analyzed by resorting to a high-fidelity Computational Fluid Dynamics (CFD) model in both design and off-design conditions, considering three speed-lines and low/high flow rate margins. Results show the capabilities and limitations of conventional low-fidelity design procedures for designing sCO_2 compressors, especially at off-design conditions, and shed light on the technical implications of the thermodynamic character of the fluid, especially in connection to the onset of phase change in the intake region of the impeller and in the tip clearance.

INTRODUCTION

The use of carbon dioxide operating in thermodynamic supercritical conditions (sCO_2) as working fluid in closed gas cycles offers the opportunity to exploit multiple classes of hot sources alternative to fossil fuels, ranging from nuclear energy [1], [2] to concentrated solar power [3] and waste heat [4], owing to the expected higher efficiency and smaller plant footprint with respect to conventional configurations such as steam or organic Rankine cycles [5], [6]. With respect to competitive technologies, sCO_2 power systems also benefit of compactness, thanks of the high density of the working fluid, which ultimately offers the opportunity of an effective control of the dynamics of the plant [7].

A key component of sCO_2 power systems is the main compressor, which is usually of centrifugal architecture and operates close to the thermodynamic critical point. The corresponding compression process allows for a significant reduction of the work required thanks to the liquid-like properties of CO_2 in these thermodynamic conditions. However, the large departure from the ideal-gas thermodynamics [8], [9], [10], as well as the potential occurrence of two-phase flows [11], [12] poses challenges in the aerodynamic design of impeller blade and meridional channel. The set-up of reliable design tools that comply with the above non-ideal effects is crucial to accelerate the development and the success of the entire technology.

Most of the studies available in Literature on sCO_2 compressors, and cited above, analyze the aerodynamics and thermodynamics of the flow within the machine or discuss the validation of computational tools for compressor flow analysis [13]. However, few works (see for example [14], [15]) focus on the design process of such non-conventional machines. In the present study, we discuss the entire design workflow of a prototype centrifugal compressor for sCO_2 applications, from the thermodynamic optimization of the cycle to the detailed definition of the meridional channel and of the blades. The study is complemented by an aerodynamic analysis of the machine in design and off-design conditions, performed by resorting to a high-fidelity CFD model which introduces the thermodynamic issues of the fluid and their aerodynamic implications.

The paper is structured as follows. At first, the energy application is defined, the thermodynamic cycle is optimized and the mean-line design of the compressor is presented. Then, the specific design guidelines for the meridional channel and the blades are introduced and applied to define the impeller. The CFD model is finally applied to assess the design and verify the compressor operation in off-design condition, also in comparison to corresponding mean-line predictions. The analysis of the two-phase flow at the impeller intake and within the tip clearance concludes the paper.

DOI: 10.17185/duepublico/73969

REFERENCE CYCLE AND COMPRESSOR TARGETS

To produce a meaningful compressor design for sCO_2 applications, preliminary cycle considerations are needed to set compressor boundary conditions and targets. Among the multitude of available cycle arrangements, the recompressed layout [5] is selected. The basic idea is to split the recuperative process downstream of the turbine in two units with different flow rates to cope with the sharp increase of the specific heat capacity at constant pressure when approaching the thermodynamic critical point. The main cycle routines and assumptions for pressure drops and pinch-point temperatures are reported in Romei *et al.* [16], in which tailored correlations that link the turbomachinery efficiencies in design conditions with cycle pressure ratio and size parameter are also provided.

For this specific task, the hot-source temperature is fixed at $T_{hs} = 550\,°C$, while the minimum cycle temperature is $T_1 = 32\,°C$. The target electrical power is $P = 50\,MW_{el}$. According to Crespi *et al.* [6], these temperature range and power can fit both nuclear and concentrating solar power applications. To derive the remaining conditions, an optimisation procedure is used to maximise the cycle electrical efficiency η_{el} by varying the minimum pressure P_1 and split factor SF, i.e. the relative amount of mass flow diverted to the second recuperator. The optimization is carried out with the `patternsearch` algorithm available in the MATLAB® Optimization toolbox. The optimization is run in a parametric way, varying the cycle pressure ratio β_{cycle} between 2 and 4 with a step of 0.25. Each optimization is run five times with a different initialization to get the global optimum at each pressure ratio. The outcome of these optimization routines are collected in the trend of the optimized efficiency against the cycle pressure ratio reported in Figure 2. The envelop of the maxima shows an optimum of the cycle efficiency for $\beta = 3.25$, which is then selected as a reference for the following compressor design.

A single-stage compressor is considered to have reduced costs and footprint. Alongside the pressure ratio, the entire cycle is determined, hence compressor requirements are wholly delineated and reported in Figure 1. In the same figure, the initial path of the corresponding isentropic compression is displayed in the T-s thermodynamic plane, highlighting the severe non-ideal effects that occur in the near-critical region in terms of the compressibility factor $Z = Pv/RT$. Moreover, the proximity of the intake conditions to the saturation curve may provoke phase

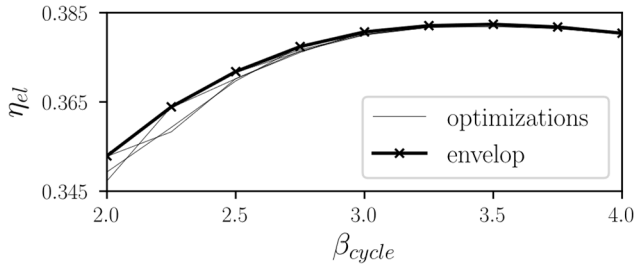

Figure 2: Trend of the optimized cycle efficiency with cycle pressure ratio.

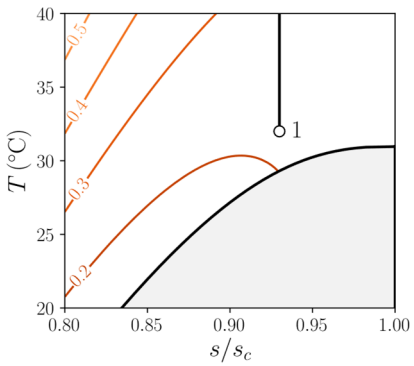

Design conditions	
P_{T1}	78.7 bar
T_{T1}	32 °C
s/s_c	0.93
β	3.25
$\dot{m}$	413.4 kg/s

Figure 1: Intake thermodynamic conditions (point 1) reported in a T-s thermodynamic plane with superposed the compressibility factor map. The two-phase domain is highlighted in gray. On the right table, compressor requirements and overall boundary conditions.

transition as a consequence of local flow accelerations, the latter proportional to the local blade loading. The saturation pressure along an isentropic expansion from the upstream thermodynamic state is $P_{sat} = 71.0\,bar$, leading to a safety margin between the intake state and saturation condition lower than ten bars. All these aspects, i.e. non-ideal effect, occurrence of two-phase flows, high blade loading, potential transonic/supersonic flow regimes, lead to an extremely complex aerodynamic design, which will be the core of the following discussions.

MEAN-LINE PRELIMINARY DESIGN

The mean-line formulation was proven to be effective for the analysis of centrifugal compressors for sCO2 applications, as widely documented in literature [2, 13, 16]. In the present study, the mean-line code was run parametrically for several design variables to seek for the highest compressor efficiency while complying with the requirements described in the previous section. A parametric study was preferred over a blind optimization technique to have track of different compressor designs with comparable performance, then making a final decision based on the minimization of phase-change triggers (e.g., blade blockage and inlet velocities).

Within a mean-line framework, pitchwise average of aerodynamic and thermodynamic quantities are computed across all component by resolving balance equations (continuity, energy and Euler equations for velocity triangles) complemented with a generalised thermodynamic treatment based on the Span-Wagner multi-parameter equation of state [17]. Relative velocities consider the radial blade evolution at the impeller inlet. As all mean-line formulations, the detailed blade shape is inherently ignored and will be discussed separately in the next section.

The performance estimates are computed by resorting to correlations that model the internal flow physics and the main sources of loss mechanism. The following loss correlations are used in this work: (i) impeller incidence [18], (ii) impeller skin-friction [19], accounting for roughness [20] and blade curvature [21] in the determination of the friction coefficient, (iii) blade

diffusion [22], (iv) tip clearance [19] corrected according to Refs. [21, 23], (v) the flow recirculation at the impeller outlet [24] (vi) mixing downstream of the impeller [25], and (vii) friction losses at the endwalls of the vaneless diffuser. The work provided by the impeller is increased to account for the recompression of a fraction of the leakage flow [26]. In this preliminary phase, the vaned diffuser and the volute are also modelled. Specifically, the vaned diffuser performance are estimated on the basis of available diffuser databooks, corrected for incidence variations in off-design performance [27]. Furthermore, the skin-friction losses are estimated in the volute, besides the dissipation of the residual radial component of the velocity at the diffuser outlet. In the following CFD analyses, these latter two components are omitted and will be discussed in future works. Finally, the impeller slip factor is estimated with the Wiesner correlation [28] corrected for the splitter blade length [20]. For sake of brevity, the detailed description of the code is not reported, however it follows standard mean-line implementations discussed in textbooks [20, 27].

As for the inlet section, the shaft diameter was determined by means of simplified mechanical calculations accounting for the transmitted power. Then, the hub diameter D_{1h} is selected assuming a safety factor of 1.08 on the shaft diameter, thus ensuring a torque transmission without mechanical issues. Given the hub diameter, the blade height b_1 was chosen to minimize the tip Mach number in the rotating frame of reference $M_{w,1t}$. During this phase, the inlet blade angle β_{1g} was constrained in the range $-80 \div -10$ deg (measured from the meridional direction, the negative sign indicates a direction opposed to the peripheral speed) to prevent an excessive flow distortion. The number of blades is varied as well, also considering splitter blades. Notwithstanding comparable performance, the splitter configuration is ultimately selected, with splitters starting at the normalized full-blade streamwise location $s_{norm} = 0.175$. This choice represents a convenient trade off between a reduction in the blade blockage at inlet and a reduction of the blade loading due to the increased blade pitch at the splitter location. The rotational speed was also part of the parametric investigation, and it was varied in the range $8000 \div 13000$ rpm.

As for the outlet section, the absolute flow angle was constrained in the range $60 \div 75$ deg; the upper limit was imposed to prevent an excessive tangential flow direction in off-design conditions, which may be responsible of earlier instabilities in the diffuser component. To this end, backward blades ($\beta_{2g} < 0$ deg) are chosen and varied in the range $-35 \div -55$ deg. Finally, an open impeller design is considered.

From this analysis, a candidate compressor was selected and depicted in Figure 3 alongside the main geometrical dimensions. At nominal conditions, the flow coefficient is $\phi = 0.021$, the peripheral Mach number $M_{u2} = 0.86$ and the peripheral Reynolds number $Re_{u2} \approx 10^9$. The shroud and hub contours are generated with ANSYS-BladeGen®, employing spline curves that pass through the geometrical quantities provided by the mean-line code. The vaned diffuser and the volute are not reported in the figure because they will be not simulated in the next section.

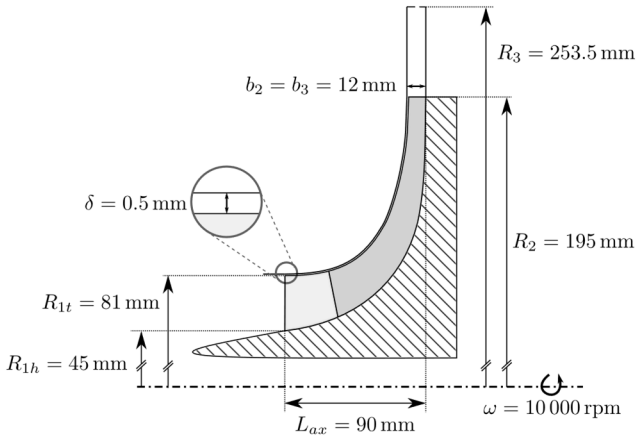

Figure 3: Meridional channel of the impeller and vaneless diffuser along with main geometrical dimensions.

The vaneless diffuser has a radial extension of 30% of the impeller radius: this value, close to the upper value of common design practices, is chosen to reduce the absolute Mach number at the vaned diffuser entrance so to ensure a good rangeability of the entire machine. For the present investigation, the vaneless pinch is neglected, but it may be included in the future to adjust the absolute flow angle when the vaned diffuser will be simulated as well.

CRITERIA FOR BLADE DESIGN

The step from a mean-line design in terms of main geometrical quantities to a complete compressor prototype requires the definition of the blade profiles and the three-dimensional stacking.

As for the blade profiles, the mean-line code provides information about the geometrical angles at the inlet and outlet section. In particular, the inlet section is split in three relevant sections, namely the hub (0% span), midspan (50% span) and tip (100% span) section. As a result of the mean-line analysis, the geometric angles at these three sections are $\beta_{1g} = -43.1, -53.7, -60.5$ deg, respectively (angles are measured from the meridional direction), assuming optimal incidence [18]. The outlet geometrical angle results $\beta_{2g} = -45$ deg. Given these boundaries, several blade angle distributions are available to pass from inlet to outlet blade angle. In the context of sCO_2 centrifugal compressor, the choice of the blade angle distribution is particularly crucial, because it directly sets the aerodynamic loading of the blade front part. The more the front blade is loaded, the more the flow locally accelerates on the suction side, the more the local thermodynamic state penetrates inside the saturation dome.

One key parameter that controls the blade loading is the wrap angle φ, i.e. the angle between the meridional plane passing through the leading edge and the one passing through the trailing edge. A low wrap-angle profile, sketched in Figure 4(a), is

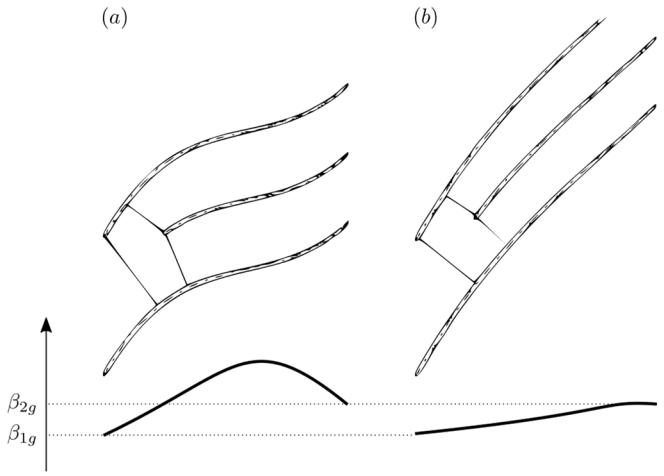

Figure 4: Influence of the wrap angle on the blade angle distribution: (*a*) low wrap-angle profile, and (*b*) high wrap-angle profile.

characterized by a limited wetted surface, thus limiting the skin-friction loss. For the same reason, the aerodynamic loading is generally high because it is concentrated on a smaller blade length. As a consequence, the fluid accelerating on the front part of the blade is more prone to phase transition. By increasing the wrap angle, the blade extends for a larger part of the circumference, hence the loading is distributed on a higher blade surface. The loading rise is generally smoother, as evidenced in Figure 4(b) for an exemplary high wrap-angle profile. Although local accelerations prompted by the aerodynamic loading are reduced in this latter configuration, the available area for the flow passage is reduced as well, see the clear reduction in the impeller throat between the two examples in Figure 4. A smaller impeller throat also promotes phase-change phenomena because the flow has to accelerate to compensate the reduction in the flow passage. At the same time, a high wrap angle contributes to a long and narrow (i.e. of small hydraulic diameter) blade channel. From this analysis, it is clear that a trade-off in the wrap angle has to be found to reduce the skin friction and diffusion losses and, at the same time, the occurrence and the extension of phase transition in sCO_2 centrifugal compressor operating in near-critical conditions. For the present design, after preliminary CFD runs, a relatively high-wrap angle is selected, i.e. $\varphi = 85$ deg.
To ease the blade manufacturability, the three-dimensional profile stacking is performed with the Flank-Milling technique. The blade thickness distribution varies linearly from 2 mm at the leading edge to 3 mm at the trailing edge regardless of the radial coordinate. The leading edge is generated with an ellipse arc with ratio among semi-axis of 2.5. The trailing edge is cut-off at R_2. Such thickness distribution results from an internal expertise, but rigorous mechanical stress analyses are planned for the near future. The final three-dimensional impeller shape is displayed in Figure 5.

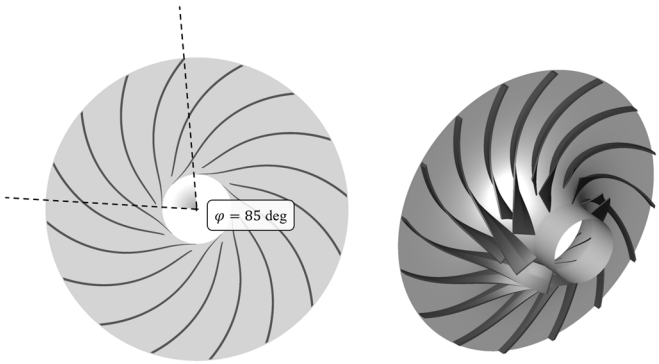

Figure 5: Three-dimensional impeller geometry.

COMPUTATIONAL FRAMEWORK

When dealing with multi-phase flows, there are several modeling strategies that can be adopted, depending on the computational cost and flow regime. The simulation of a highly loaded centrifugal compressor operating with CO_2 in near critical conditions represents an extremely challenging case from the computational perspective (complex thermodynamics coupled with high-speed flows in a rotating reference frame), hence the simulation tool needs to balance the solution accuracy with computational efficiency and robustness.

To this end, a two-fluid flow representation (with reference to the Brennen's classification [29]) is employed in the present work, named *barotropic model*, which also assumes that (i) the phases are in thermal and mechanical equilibrium, and (ii) any thermodynamic/transport property of the mixture Ψ only depends on the pressure, e.g. $\Psi = \Psi(P)$. Owing to the barotropic assumption, the equation of state is simply $\rho = \rho(P)$. In this work, such relationship is interpolated from the REFPROP® estimate at the upstream isentrope, referring to the thermodynamic equilibrium mixture density when the isentrope crosses the saturation curve. As the intake conditions are close to the critical point, meta-stability effects are neglected in the determination of the barotropic equation of state. The resulting functional trend for this specific thermodynamic condition is represented by the black curve in Figure 6. As the equation of state does not depend on thermal quantities, the equations of motion are decoupled from the energy equation, which does not

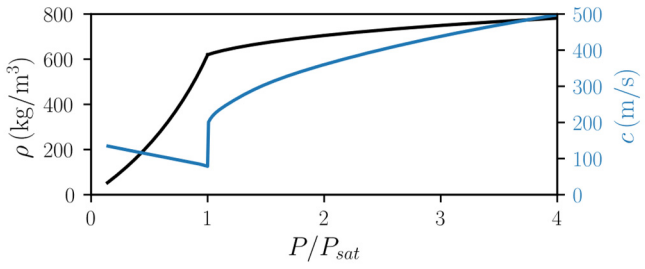

Figure 6: Barotropic equation of state $\rho = \rho(P)$ and corresponding speed of sound.

need to be explicitly resolved. The speed of sound in both single- and two-phase domain is computed as derivative of the barotropic equation of state, i.e. $c = \sqrt{(\partial P/\partial \rho)_s}$. The kink in the density curve at the saturation pressure translates in a jump of the speed of sound (blue curve in Figure 6), which is more than halved when phase change initiates. This result is aligned with the homogeneous equilibrium theory [30]. An average molecular viscosity between the inlet and outlet state is also provided. Finally, the two-equation turbulence model $k-\omega$ SST [31] closes the Reynolds-averaged Navier-Stokes (RANS) equations.

The barotropic model is implemented in ANSYS-CFX® following the procedure outlined in Persico *et al.* [12], which uses a logistic function to interpolate separately the two branches (in the single-phase and in the two-phase regions) of the barotropic function reported in Figure 6. The barotropic model was validated against the experiments of Nakagawa *et al.* [32], which were carried out for supercritical intake thermodynamic conditions close to the ones considered in the present study. The overall agreement was found to be remarkable from both the qualitative and quantitative point of views, revealing pressure differences between experiment and simulations of the order of 2% [12]. This assessment qualifies the model as adequate for simulating compressible two-phase flows within sCO2 turbo-compressors, in which the heat transfer can be neglected.

Simulations were performed assigning at the inlet the total pressure, purely meridional flow, turbulence intensity equal to 5% and eddy viscosity ratio equal to 1; at the outlet, the mass flow rate was assigned at the design flow coefficient, while an average static pressure, accepting 5% of tolerance across the outlet surface, is assigned and varied each time to generate the off-design performance maps. No-slip boundary conditions are imposed to the solid walls, also assuming a grain-sand roughness of $6.2\,\mu m$. Counter-rotating boundary conditions are also assigned both at the shroud to simulate an open impeller with a normal tip clearance $\delta = 0.5mm$ and at the vaneless diffuser (stationary component). Finally, periodic boundary conditions are exploited to simulate a single flow passage containing both the main and the splitter blade. High-resolution numerical schemes are used in the discretization of the flow advection term, while second-order central difference scheme for the diffusion term. The advection term in turbulence equations is discretized with a first-order upwind scheme.

Meshes are generated with ANSYS-Turbogrid®. Three hexahedral meshes are considered with an increasing number of elements, allocated as in Table 1. A cell clustering is imposed close to the walls, with a first layer distance approximately equal to the sand-grain roughness, thus resorting to modified wall function to properly account for the roughness effects. In terms of integral quantities, only small differences are found among the three meshes, with a maximum discrepancy in terms of total-to-total efficiency of 0.1 percentage point between the coarse and the fine mesh. Some visible differences are found in the resolution of the flow field, especially in the front part of the blade where two-phase supersonic flows are established. The results are summarized in Figure 7, where the blade loading of the main and splitter blade is reported for the three meshes. The medium mesh closely follows the trends of the finer mesh, while the coarse mesh considerably smooths the loading distribution in the front part of the blades, although recovering a good agreement afterwards. The medium mesh is ultimately selected for the following analyses as it provides a complete flow description at the minimum computational cost.

	Coarse	Medium	Fine
Hub BL	9	13	18
Shroud BL	9	13	18
Tip Clearance	9	18	28
Overall span	40	70	100
Bl2Bl Impeller	25,000	75,000	150,000
Overall	1.9×10^6	8.8×10^6	2.4×10^7

Table 1: Cell distribution for the grid assessment.

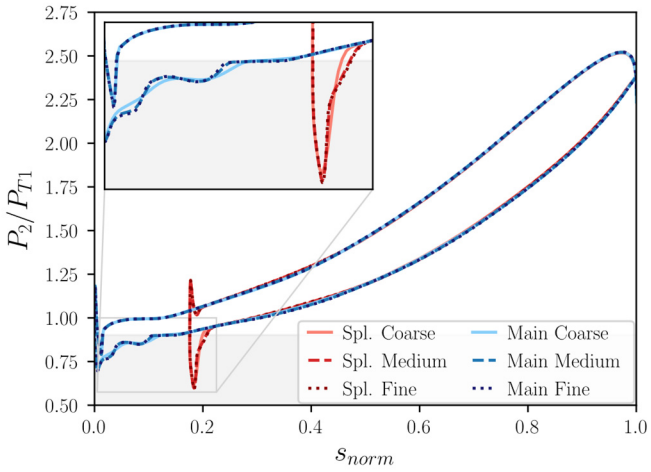

Figure 7: Blade loading distributions of the main and splitter blade at midspan for different grid refinements. The gray area identifies the region $\boldsymbol{P < P_{sat}}$, where $\boldsymbol{P_{sat}}$ is the saturation pressure obtained through an isentropic transformation.

COMPRESSOR PERFORMANCE

The compressor performances are analyzed for three representative speedlines, namely 60%, 80% and 100% of the nominal one. For these speeds, the peripheral Mach number is $M_{u2,des} = 0.52, 0.69, 0.86$, respectively. The wide range of rotational speed is chosen to ensure an adequate flexibility of the power cycle in off-design conditions. The performance map in terms of total-to-total pressure ratio and efficiency are reported in Figure 8, in which CFD predictions are compared with the original mean-line estimates. The pressure ratio agreement is remarkable, with no relevant differences among the two methodologies. It has to be noted that the design pressure ratio is slightly higher the one required by the cycle (3.46 against the

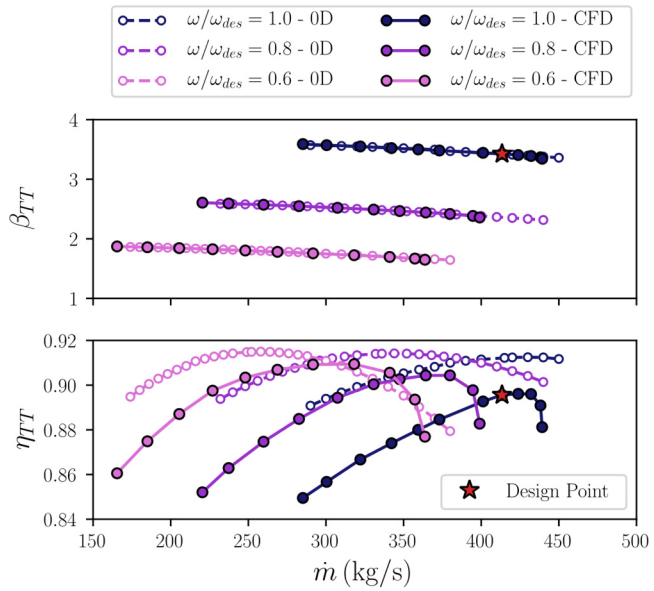

Figure 8: Performance maps of the centrifugal compressor obtained with CFD simulations and mean-line analyses.

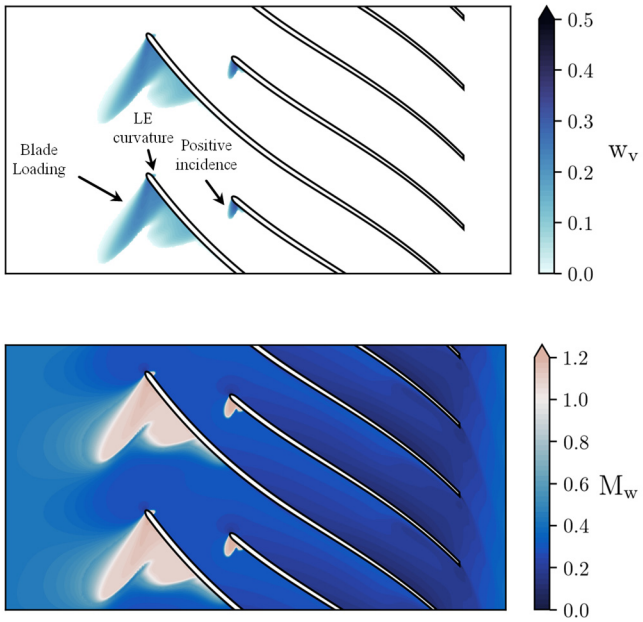

Figure 9: Vapor mass-fraction (top) and relative Mach number (bottom) flow field in the blade-to-blade plane at midspan (50%) for design flow coefficient and rotational speed.

required 3.25) because the vaned diffuser and the volute are not included in the present analysis. Larger discrepancies are found in the efficiency predictions, with errors of the order of 2 percentage point, aligned and even better than other mean-line results [33, 34]. The mean trend of the efficiency curve is generally captured except at high flow rate for the speedline at 80% and 100%. From a similitude perspective, one might expect similar behavior across the operational range owing to the high Reynolds number ($Re_{u2} > 5 \times 10^8$ for the lowest rotational speed) and small contribution of the compressibility (in these thermodynamic conditions, the CO_2 behaves in a liquid-like manner, with only marginal variation of the ratio ρ_2/ρ_1 across the three speedlines at given flow coefficient).

The underlying reason for the abrupt drop in the efficiency trend at high flow rates when the rotational speed increases is the role of multi-phase effects. The distribution of vapor mass fraction on the blade-to-blade plane at midspan is reported in Figure 9 for the design conditions. Three regions in which cavitation occurs (transition from liquid to vapor phase driven by pressure) can be recognized: (i) a wider region on the front suction side of the main blade induced by the local aerodynamic loading, (ii) a tiny region on the front pressure side given by the flow acceleration around the elliptic leading edge, and (iii) a small region on the splitter suction side, mainly provided by a positive incidence on the splitter blade. All these features can also be recognized in the blade loading in Figure 7. The vapor mass fraction in these regions can reach values of the order of 30%. Notice that, given the combination of high pressure ratio and operation in the near-critical region, the occurrence of cavitation is in practice unavoidable. However, from a mechanical perspective, the cavitation is expected to be less harmful than what usually occurs in conventional turbopumps, because the density ratio between the two phases in these conditions is at least one order of magnitude smaller. In correspondence of the multi-phase zones, the relative Mach number, reported in the same figure, shows a sudden increase; the flow regime passes from highly subsonic ($M_w < 1$ in the blue

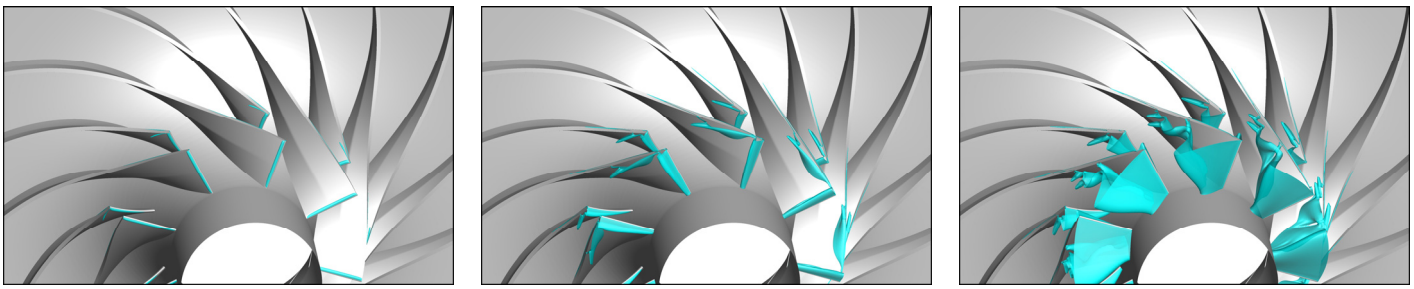

(a) $\phi/\phi_{des} = 1, \omega/\omega_{des} = 0.6$ (b) $\phi/\phi_{des} = 1, \omega/\omega_{des} = 0.8$ (c) $\phi/\phi_{des} = 1, \omega/\omega_{des} = 1.0$

Figure 10: Extension of the two-phase region for the design flow coefficient at different rotational speed.

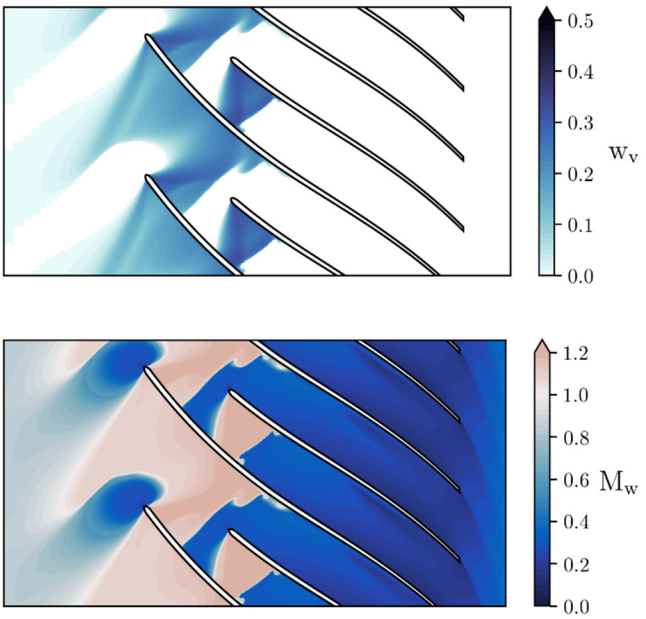

Figure 11: Vapor mass-fraction (top) and relative Mach number (bottom) flow field in the blade-to-blade plane at midspan (50%) for $\phi/\phi_{des} = 1.06$ and $\omega/\omega_{des} = 1.0$.

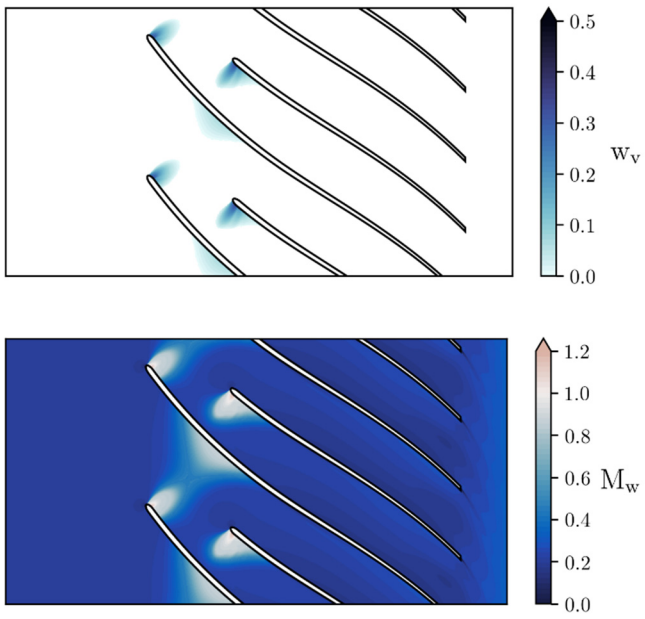

Figure 12: Vapor mass-fraction (top) and relative Mach number (bottom) flow field in the blade-to-blade plane at midspan (50%) for $\phi/\phi_{des} = 1.38$ and $\omega/\omega_{des} = 0.6$.

region) to supersonic ($M_w > 1$ in the red region) when the flow transits. This phenomenon is strictly related to the behavior of the sound speed under the assumption of thermodynamic equilibrium, as already explained in Figure 6.

The occurrence and the amount of phase change is strictly related to the flow aerodynamics. The higher the target pressure ratio, the larger the blade loading and the accelerations involved. Therefore, when reducing the rotational speed, the velocities are generally lower, as well as the resulting blade loading and pressure ratio. The influence of the rotational speed on the two-phase region extent is reported in Figure 10. At the nominal rotational speed, the two-phase region interests the whole span, manly developing on the main blade suction side. When the rotational speed is 80% of the design one, the region dramatically reduces in its extent, although it still develops on the whole span. The larger region is located at the tip region, where the relative velocities are higher. Finally, moving to the lowest rotational speed, i.e. 60% of the design one, the two-phase region is almost completely suppressed, and the only contribution to its generation is provided by the leading-edge curvature. Indeed, at this rotational speed the acceleration of the flow on the suction side is not prompting the phase transition.

Up to now the discussion focused on the design flow rate. Analogous considerations apply when moving along the same speedline. In particular, when the flow rate increases, the velocities are generally higher to cope with the large amount of flow to be delivered. In this context, the phase-change phenomena are more prominent. As a consequence, at nominal speed the right limit (choking limit) on the compressor map is found at 106% of the design flow rate. For this case, the flow field at midspan is reported in Figure 11. It can be readily recognized that the phase change affects the whole blade channel, there inducing a supersonic Mach number. Specifically, a region vapor-free is observed at the leading edge where the flow impinges on the blade. In this zone, the velocity goes to zero and the static pressure approaches the design total pressure, which is above the saturation limit. However, both the suction and the pressure side are severely affected by two-phase flows. At flow rates larger than the nominal one, the flow approaches the blade with a negative incidence, that causes a consistent acceleration right after the leading edge to recover the blade angle direction. In this location, the flow meets the flow coming from the adjacent blade suction side, which also undergoes to phase transition due to local acceleration on the blade surface. Such flow accelerations are sufficient to affect the whole blade channel, hence inducing a choked compressor operation. An analogous flow field is also found at the hub profile, confirming that the whole machine is choked.

At the lowest rotational speed, the operating range extends up to 145% of the nominal flow. To show the impact of two-phase flow at this rotational speed, the flow field at midspan is reported in Figure 12 for a mass flow rate increased by 38% with respect to the design one. As a result of a lower rotational speed and, by velocity triangles composition, of overall lower relative velocities, the two-phase regions are significantly reduced compared to those in Figure 11. In these conditions, the two-

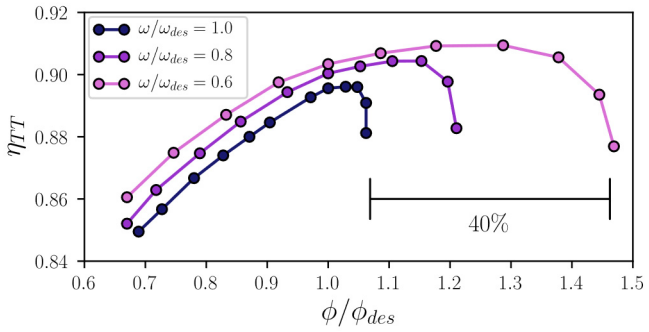

Figure 13: Dimensionless performance maps in terms of flow coefficient and total-to-total efficiency.

phase flow is mainly triggered by incidence effect, which prompts a localized acceleration on the pressure side. The flow on suction side also undergoes to phase change, but the two zones are not connected, hence the free-stream remains in single phase with a Mach number considerably lower than the unity.

At low flow rates, the phase transition is hampered by the low relative velocities, although localized two-phase regions can also be established because of a positive incidence angle [12]. However, their contribution seems to be marginal to the determination of the left operational limit (surge line), which is still determined by an excessive flow diffusion that causes flow instabilities in the impeller channel.

Finally, the aerodynamic analyses described in this section demonstrated that two-phase effects influence the compressor operational range by limiting the right limit, as further clarified by Figure 13. Specifically, the onset of phase transition sets an early choking of the compressor, reducing the operational range of about 40% with respect to phase-change-free operation. Moreover, as phase transition is mainly prompted by local effects (blade loading, incidence) rather than global effects that affect the free stream (e.g., blade blockage), conventional mean-line codes are not able to predict this early reduction in operational range, as visible by the comparison between mean-line and CFD predictions at the nominal speed in Figure 8.

Tip clearance

In the previous section it was pointed out that the onset of phase change in these specific thermodynamic conditions promotes supersonic flow regime and choking operation. Notwithstanding the detrimental effect on the compressor range, the trigger of choking may be used to some extent to limit the leakage flow rate in the design of open impellers. Moreover, as the leakage flow is localized in the tip section, the relative velocities are higher and, consequently, two-phase effects are also more prominent, as also evidenced in Figure 10.

The streamlines are reported for the design case in Figure 14. The sonic iso-surface shows that the tip leakage features a supersonic flow regime in the initial part of the main and splitter blade. Analogous streamlines are extracted for the other speedlines at the design flow coefficient; the sonic region is reduced when the rotational speed is 80% of the nominal one,

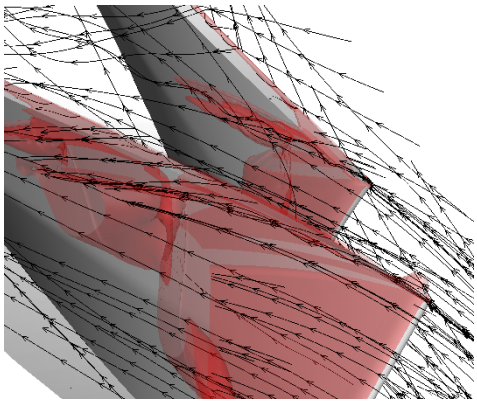

Figure 14: Streamlines at the design flow coefficient and rotational speed. In red, the iso-surface $\boldsymbol{M_w = 1}$ is reported.

while it is practically absent for the lowest rotational speed, in which the two-phase region is prompted only by the flow curvature around the leading edge. The relative amount of the total flow rate passing through the gap of the main and splitter blade is 17.6%, approximately equal for the three cases under examination. The same relative amount of leakage seemingly suggest that the occurrence of sonic conditions prompted by the onset of two-phase flows has not a relevant effect on the leakage and on the corresponding losses. As a conclusive remarks, it is worth to underline that the present computational methodology only considers the different compressibility between the single- and two-phase fluid under mechanical and thermodynamic equilibrium assumption, without accounting for heterogeneous and phase-change effects on the frictional coefficient [29] that may instead play a role in the interstitial gap.

CONCLUSION

The paper discusses the design process and the computational assessment of a prototype centrifugal compressor for sCO_2 applications. Starting from the optimization of the thermodynamic cycle to derive realistic boundary conditions and requirements, a single-stage highly loaded compressor (pressure ratio greater than 3) was introduced, discussing the peculiar design of sCO_2 compressors operating in the near-critical region. In particular, the discussion focused on the blade-design strategies to minimize the front loading, with the aim of minimizing the onset of phase change at the compressor intake.

The resulting three-dimensional compressor configuration was analyzed in design and off-design conditions using both a low-fidelity mean-line tool and a high-fidelity CFD model. Results confirmed the expected compressor performance in design conditions, with the two simulations tools showing excellent agreement in terms of pressure ratio and reasonable agreement in terms of efficiency (differences within 1.5–2%). However, the CFD simulations showed wide regions potentially exposed to cavitation, prompting there supersonic flow regime because of the drop in the speed of sound when the

thermodynamic state falls in the two-phase domain. Starting from such a severe configuration at nominal flow rate, choking quickly occurs as soon as the compressor is operated at higher flow rate (106% of the nominal value) due to the enlargement of the two-phase region to the whole intake of the machine. This effect, originated by the front loading and by the incidence on the main and splitter blades, cannot be captured by the low-fidelity tool, which overestimates the choked-flow condition with respect to the CFD prediction.

As the angular speed is reduced, the compressor loading reduces as well, and the above effects progressively weakens. Consequently, the agreement between the mean-line and CFD predictions greatly improves at high flow rate too. For the lowest angular speed, the onset of phase change is limited in local areas close to the leading edge due to blade curvature and it has not a relevant effect on the compressor performance. As a result, the free-stream does not undergo to phase change even at high flow rate, hence the compressor range is increased of about 40% with respect to the nominal rotational speed, in which phase-change effects are prominent. Finally, although the tip clearance is also affected by phase-change phenomena at the nominal speed, the relative fraction of flow rate passing through the clearance remains practically unaltered compared to cases at a lower rotational speed in which only single-phase flows are detected in the interstitial gap.

This study has shown that the compressor loading drives the phase change, which cannot be eliminated even by resorting to tailored design strategies. The onset of phase change has a relatively weak impact on the compressor efficiency (at least in according to the present computational methodology, that neglects the entropy produced during the phase transition), but it strongly reduces the right operation limit of the compressor. High-fidelity CFD tools are required to properly master this effect. Future works will also include the vaned diffuser and the volute in the design chain, besides analyzing off-design operation of the compressor when the intake thermodynamic conditions are varied.

NOMENCLATURE

Acronym

BL	boundary layer
Bl2Bl	blade-to-blade plane
sCO_2	supercritical carbon dioxide
CFD	computational fluid dynamics
RANS	Reynolds-averaged Navier-Stokes

Roman Symbol

c	speed of sound
h	specific enthalpy
$\dot{m}$	mass flow rate
M	Mach number
M_{u2}	peripheral Mach number u_2/c_{T1}
M_W	relative Mach number
P	pressure
Re_{u2}	peripheral Reynolds number $\rho_{T1}u_2D_2/\mu_{T1}$
s	specific entropy
s_{norm}	normalized streamwise direction
T	temperature
v	absolute velocity
w	relative velocity
w_v	vapor mass fraction
Z	compressibility factor

Greek Symbol

β	pressure ratio
β_g	impeller blade angle
δ	tip clearance
ϕ	flow coefficient $\dot{V}/(u_2D_2^2)$
φ	wrap angle
η	isentropic efficiency
η_{el}	net cycle efficiency
μ	molecular viscosity
ω	rotational speed
ρ	density

Subscripts

$(\cdot)_c$	critical condition
$(\cdot)_{des}$	design condition
$(\cdot)_{sat}$	saturation (at fixed entropy)
$(\cdot)_T$	total condition
$(\cdot)_{TT}$	total-to-total
$(\cdot)_1$	impeller inlet/midspan
$(\cdot)_{1h}$	impeller hub
$(\cdot)_{1t}$	impeller tip
$(\cdot)_2$	impeller outlet
$(\cdot)_3$	vaneless diffuser outlet

REFERENCES

[1] V. Dostal, A Supercritical Carbon Dioxide Cycle for Next Generation, Ph.D. thesis, Massachusetts Institute of Technology, 2004.

[2] J. Lee, J. I. Lee, H. J. Yoon and J. E. Cha, "Supercritical Carbon Dioxide Turbomachinery Design for Water-Cooled Small Modular Reactor Application," *Nucl. Eng. Des.,,* vol. 270, pp. 76-89, 2014.

[3] T. Neises and C. and Turchi, "A Comparison of Supercritical Carbon Dioxide Power Cycle Configurations With an Emphasis on CSP Applications," *Energy Procedia,* vol. 49, p. 1187–1196, 2014.

[4] M. Marchionni, G. Bianchi and S. Tassou, "Review of supercritical carbon dioxide (sCO2) technologies for high-grade waste heat to power conversion," *SN Applied Sciences,* vol. 2, no. 611, 2020.

[5] G. Angelino, "Carbon dioxide condensation cycles for power production," *ASME Paper No. 68-GT-23, J. Eng. Power 90,* 1968.

[6] F. Crespi, G. Gavagnin, D. Sanchez and G. S. Martinez, "Supercritical carbon dioxide cycles for power generation: A review," *Applied Energy,* pp. 152-183, 2017.

[7] M. Marchionni, L. Chai, G. Bianchi and S. Tassou, "Numerical modelling and transient analysis of a printed circuit heat exchanger used as recuperator for supercritical CO2 heat to power conversion systems," *Applied Thermal Engineering,* vol. 161, no. 114190, 2019.

[8] S. A. Wright, R. F. Radel, M. E. Vernon, G. E. Rochau and P. S. Pickard, *Operation and Analysis of a Supercritical CO2 Brayton Cycle,* Sandia Report SAND2010-0171, 2010.

[9] J. S. Noall and J. J. Pasch, "Achievable Efficiency and Stability of Supercritical CO2 Compression Systems Main Compressor

Design Discussion," in *The 4th International Symposium—Supercritical CO2 Power Cycles*, Pittsburgh, PA, USA, 2014.

[10] N. D. Baltadjiev, C. Lettieri and Z. S. Spakovszky, "An investigation of real gas effects in supercritical CO2 centrifugal compressors," *Journal of Turbomachinery,* vol. 137, 2015.

[11] A. Hosangadi, Z. W. T. Liu, V. Ahuja and J. Busby, "Modeling Multiphase Effects in CO2 Compressors at Subcritical Inlet Conditions," *Journal of Engineering for Gas Turbines and Power,* vol. 141, 2019.

[12] G. Persico, P. Gaetani, A. Romei, L. Toni, E. F. Bellobuono and R. Valente, "Implications Of Phase Change On The Aerodynamics Of Centrifugal Compressors For Supercritical Carbon Dioxide Applications," in press in the *Journal of Engineering for Gas Turbines and Power*, 2021.

[13] A. Ameli, T. Turunen-Saaresti and J. Backman, "Numerical investigation of the flow behavior inside a supercritical CO2 centrifugal compressor," *Journal of Engineering for Gas Turbines and Power ,* vol. 140, no. 6, p. 122604, 2018.

[14] A. Hacks, S. Schuster, H. J. Dohmen, F. K. Benra and D. Brillert, "Turbomachine Design for Supercritical Carbon Dioxide Within the sCO2-HeRo.eu Project," *Journal of Engineering for Gas Turbines and Power,* vol. 140, 2018.

[15] R. Pelton, T. Allison, S. Jung and N. Smith, "Design of a Wide-Range Centrifugal Compressor Stage for Supercritical CO2 Power Cycles," in *ASME Turbo xpo 2017*, Charlotte, NC, USA, 2017.

[16] A. Romei, P. Gaetani, A. Giostri and G. Persico, "The role of turbomachinery perfomance in the optimization of supercritical carbon dioxide power systems," *Journal of Turbomachinery,* vol. 142, no. 7, p. 071001, 2020.

[17] R. Span and W. Wagner, "A New Equation of State for Carbon Dioxide Covering the Fluid Region from the Triple-Point Temperature to 1100 K at Pressures up to 800 MPa," *Journal of Physical and Chemical Reference Data,* vol. 25, no. 6, pp. 1509-1596 , 1996.

[18] M. R. Galvas, "FORTRAN program for predicting off-design performance of centrifugal compressors," NASA TN D-7487, 1973.

[19] W. Jansen, "A method for calculating the flow in a centrifugal compressor impeller when entropy gradients are present," in *Royal Society conference on internal aerodynamics (turbomachinery)*, 1967.

[20] R. H. Aungier, Centrifugal Compressors: a strategy for aerodynamic analysis and design, New York: ASME Press, 2000.

[21] D. S. Musgrave, "The prediction of design and off-design efficiency for centrifugal compressor impellers," *ASME 22nd fluids engineering conference,* 1980.

[22] C. Rodgers, " A Diffusion Factor Correlation for Centrifugal Impeller Stalling," *J. Eng. Power,* vol. 100, no. 4, pp. 592-601, 1978.

[23] J. J. Brasz, "Investigation Into the Effect of Tip Clearance on Centrifugal Compressor Performance," in *ASME 1988 International Gas Turbine and Aeroengine Congress and Exposition*, Amsterdam, The Netherlands, 1988.

[24] J. E. Coppage, F. Dallenbach, H. Eichenberger, G. E. Hlavaka, E. M. Knoernschild and N. Van Lee, "Study of supersonic radial compressors for refrigeration and pressurization systems," WADC report 55-257, 1956.

[25] J. P. Johnston and R. C. Dean, "Losses in vaneless diffusers of centrifugal compressors and pumps," *Trans. ASME Journal of Engineering for Power,* pp. 49--62, 1966.

[26] R. H. Aungier, "Mean Streamline Aerodynamic Performance Analysis of Centrifugal Compressors," *Journal of Turbomachinery,* vol. 117, no. 3, pp. 360-366, 1995.

[27] A. Whitfield and N. Baines, Design of radial turbomachines, Logman Singapore Publishers Ltd., 1990.

[28] F. J. Wiesner, "A Review of Slip Factors for Centrifugal Impellers," *Trans. ASME: J. Eng. Gas Turbines Power,* pp. 558--572, 1967.

[29] C. E. Brennen, Fundamentals of Multiphase Flows, Cambridge University Press, 2005.

[30] M. De Lorenzo, P. Lafon, J. M. Seynhaeve and Y. Bartosiewicz, "Benchmark of Delayed Equilibrium Model (DEM) and classic two-phase critical flow models against experimental data," *International Journal of Multiphase Flow,* vol. 92, pp. 112-130, 2017.

[31] F. R. Menter, "Two-Equation Eddy-Viscosity Turbulence Models for Engineering Applications," *AIAA Journal,* vol. 32, no. 8, pp. 1598-1605, 1994.

[32] M. Nakagawaa, M. Serrano Beranaa and A. Kishinec, "Supersonic two-phase flow of CO2 through converging–diverging nozzles for the ejector refrigeration cycle," *International Journal of Refrigeration,* vol. 32, pp. 1195-1202, 2009.

[33] A. Meroni, B. Zühlsdorf, B. Elmegaard and F. Haglind, "Design of Centrifugal Compressors for Heat Pump Systems," *Applied Energy,* vol. 232, pp. 139-156, 2018.

[34] J. Schiffmann and D. Favrat, "Design, experimental investigation and multi-objective optimization of a small-scale radial compressor for heat pump applications," *Energy,* vol. 35, no. 1, pp. 436-450, 2009.

DOI: 10.17185/duepublico/73969
URN: urn:nbn:de:hbz:464-20210330-113422-0